Journal of Structural Geology 30 (2008) 888–898

Contents lists available at ScienceDirect

Journal of Structural Geology

journal homepage: www.elsevier.com/locate/jsg

Early stage evolution of growth faults: 3D seismic insights from the Levant Basin, Eastern Mediterranean

Catherine Baudon*, Joe Cartwright

3D Lab, School of Earth, Ocean and Planetary Sciences, Cardiff University, Main Building, Park Place, Cardiff, CF10 3AT, UK

ARTICLE INFO

Article history:
Received 12 March 2007
Received in revised form 22 February 2008
Accepted 26 February 2008
Available online 8 March 2008

Keywords:
Growth fault
Blind propagation
Throw distribution
Fault nucleation
Segmentation

ABSTRACT

The geometry and kinematic evolution of small growth faults were analysed from a high-resolution 3D seismic dataset located at the margins of the Levant Basin, in the eastern Mediterranean. The 3D geometry, segmentation history and throw distribution of one particular fault was reconstructed to evaluate and illustrate the changes in dimension and displacement distribution that occurred during the transition from purely blind propagation to propagation at the free surface. The fault is considered to have grown by blind radial propagation of three main segments that hard-linked prior to surface interaction. The fault subsequently reached the seabed and continued to accrue displacement as a syn-sedimentary fault. Most of the fault surface area formed during the blind propagation phase, but most of the displacement was added during the syn-sedimentary phase of the growth history with little increase in surface area. The interaction of the fault with the free surface led to a change in the position of the point of maximum displacement as well as modifying the vertical throw distribution. The amount of displacement added after this transition from blind fault to growth fault is discussed with respect to existing fault-growth models.

1. Introduction

Growth faults have been the subject of extensive research, mainly with an aim of defining their tectono-stratigraphical evolution in the context of a local petroleum systems analysis (e.g. Ocamb, 1961; Bruce, 1973; Crans et al., 1980). In shelf and upper slope environments where sedimentation rates often keep pace with fault displacement rates (e.g. Cartwright et al., 1998; Castelltort et al., 2004; Back et al., 2006), stratigraphic thickness changes across growth faults enable the throw that accumulated during deposition to be calculated (e.g. Thorsen, 1963; Edwards, 1995). However, small syn-sedimentary faults can be extremely difficult to distinguish from blind faults i.e. those that grew by blind propagation with no interaction with the free surface at any point during their evolution (e.g. Watterson, 1986; Petersen et al., 1992; Childs et al., 1993; Nicol et al., 1996). This difficulty arises because the overall distribution of displacement on blind faults and small syn-sedimentary faults can be identical. Whereas for a syn-sedimentary fault, the upwards decrease in throw reasonably equates to a minor stratigraphic expansion across the fault (Thorsen, 1963), for a blind fault the upwards decrease relates to a propagation gradient (Walsh and Watterson, 1987).

Syn-sedimentary faults will almost invariably experience a degree of propagation as a blind fault, since propagation of the upper tip to the free surface necessarily proceeds whilst the tip line propagates laterally and downward in a blind manner (Meyer et al., 2002; Childs et al., 2003). Very few faults nucleate at the free surface, which is not surprising, given the small confining stress at the surface combined with the typically high porosity and low shear strengths of near-surface sediments.

Little is known about fault propagation once free surface interaction occurs along the upper tip, including changes in fault displacement distribution and dimension. Therefore, a need exists to investigate the characteristics of blind versus syn-sedimentary propagation and the transition between the two faulting stages. The relationship between blind and syn-sedimentary modes of fault propagation is also important to understand in the context of fault scaling. It has been suggested recently, that the along-strike length of normal faults can be established at an early stage of fault evolution and hence, further displacement is added without change in fault length (e.g. Morewood and Roberts, 1999; Poulimenos, 2000; Meyer et al., 2002; Walsh et al., 2002; Nicol et al., 2005; Vetel et al., 2005). These studies interpreted approximately constant fault length as inherited by reactivation of pre-existing fault planes. It is interesting to consider whether such a two-stage growth model also applies to newly propagating faults in previously undeformed settings.

* Corresponding author. NARG, SEAES, The University of Manchester, Oxford Road, Williamson Building, Manchester, M13 9PL, UK. Tel.: +44 (0) 161 275 0778; fax: +44 (0) 161 306 9361.
E-mail address: catherine.baudon@manchester.ac.uk (C. Baudon).

0191-8141/$ – see front matter © 2008 Elsevier Ltd. All rights reserved.
doi:10.1016/j.jsg.2008.02.019

The aims of this study are to investigate and characterise the early propagation history of growth faults that recently made the transition from a blind to a syn-sedimentary stage, and to evaluate the implications for existing fault-growth models and scaling relationships. The main focus of this study is a single, segmented fault located in an array of simple gravity-driven extensional faults mapped on a high quality 3D seismic survey located at the margin of the Levant Basin in the eastern Mediterranean. This fault was selected for its relatively simple geometry and a kinematic history that straddles the transition from blind to syn-sedimentary propagation. The paper concludes with a discussion of the wider importance of this kinematic progression.

2. Geological setting and dataset

2.1. Regional setting

The study area is located in the Levant Basin, in a passive continental margin setting in the eastern Mediterranean (Fig. 1). The basin formed through several phases of rifting from the Early Permian to the Middle Jurassic and is associated with the evolution of the Neo-Tethys Ocean (Garfunkel, 1998). The Levant Basin has been influenced by its location at the zone of interaction between the Anatolian, African and Arabian plates and is bounded by the Dead Sea Transform to the East, the Gulf of Suez to the SW and the Cyprian Arc to the NW (Tibor and Ben-Avraham, 2005) (Fig. 1a).

Tectonic uplift of the shelf associated with a subsidence of the slope and basin during the Miocene (Frey Martinez et al., 2005) led to an increase in siliciclastic sediment supply (Druckman et al., 1995). At the end of the Miocene, major drawdown of sea level occurred in the Levant Basin as part of the Messinian Salinity Crisis (MSC) (Hsü et al., 1978). This change led to extensive erosion and deposition of thick evaporites, bounded by Horizons M and N, in the basin floor regions (Tibor and Ben-Avraham, 1992) pinching out laterally against the basin margins (Bertoni and Cartwright, 2006) (Fig. 1b). A major transgression and re-establishment of normal marine conditions at the beginning of the Pliocene led to the deposition of an interval of turbidite sandstones named the Yafo Sand Member (YSM) (Frey Martinez et al., 2005).

The Plio–Pleistocene succession that overlies the Miocene–Oligocene sediments forms the main interval of interest of this paper (Fig. 2). The interval is characterised by continuous moderate to high-amplitude seismic reflections alternating with chaotic low-amplitude reflection packages that have been interpreted as slump deposits (Frey Martinez et al., 2005). These sediments are mostly clay-rich marls, sandstones and claystones deposited in a slope position and mainly derived from the Nile Delta (Tibor and Ben-Avraham, 1992). Tilting of the margin resulted in two scales of gravity-driven deformation during the Pliocene: thin-skinned landslides (Frey Martinez et al., 2005) and extensional gravity spreading of the succession detaching in the Messinian evaporites (Garfunkel and Almagor, 1987; Netzeband et al., 2006; Cartwright and Jackson, 2008). The extensional domain occupies the modern shelf and upper slope of the basin and is characterised by a series of downslope and upslope dipping extensional faults localised above and generally detaching into the pinch-out zone of the Messinian evaporites (Bertoni and Cartwright, 2006; Cartwright and Jackson, 2008) (Figs. 3 and 4).

2.2. Dataset and methodology

This study is based on a high-resolution 3D seismic survey located in the southern part of the Levant Basin (Fig. 1), supplemented by a regional 2D reflection survey covering the continental margin of offshore Israel. The 3D survey covers an area of 2200 km^2, with a frequency range between 35 Hz and 80 Hz and a dominant frequency of 50 Hz at the base of the Pliocene, giving a vertical resolution of c. 10 m. The spatial resolution is approximately equivalent to the in-line and the cross-line spacing of 25 m. Ten exploration wells were drilled within the survey area and provide standard petrophysical and velocity data for use in lithological interpretation and in time-to-depth conversion.

Regional horizon mapping at up to 14 different stratigraphic levels and fault interpretation were undertaken using

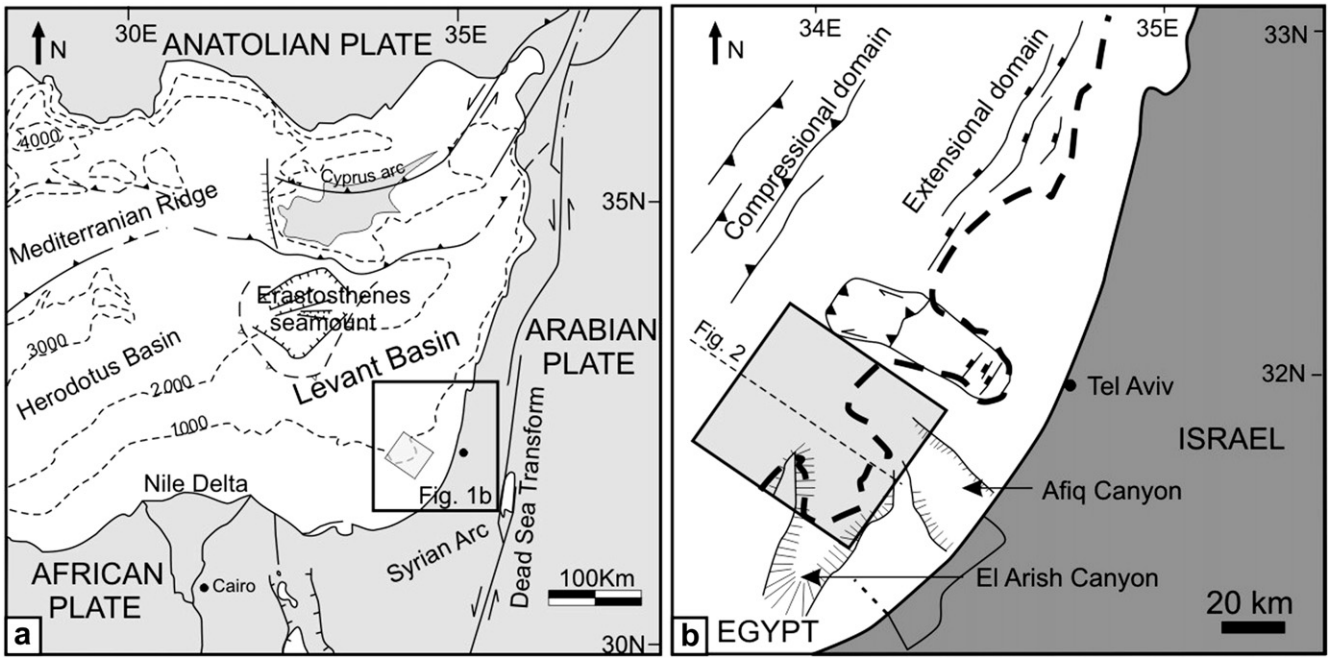

Fig. 1. Schematic maps of the study area (a) showing the major structures of the Eastern Mediterranean, modified after Garfunkel, 1998. Dashed lines indicate the bathymetry (b) showing the location of the 3D seismic survey (shaded square) situated offshore Israel. Thick dashed line represents the margin of the Messinian evaporites.

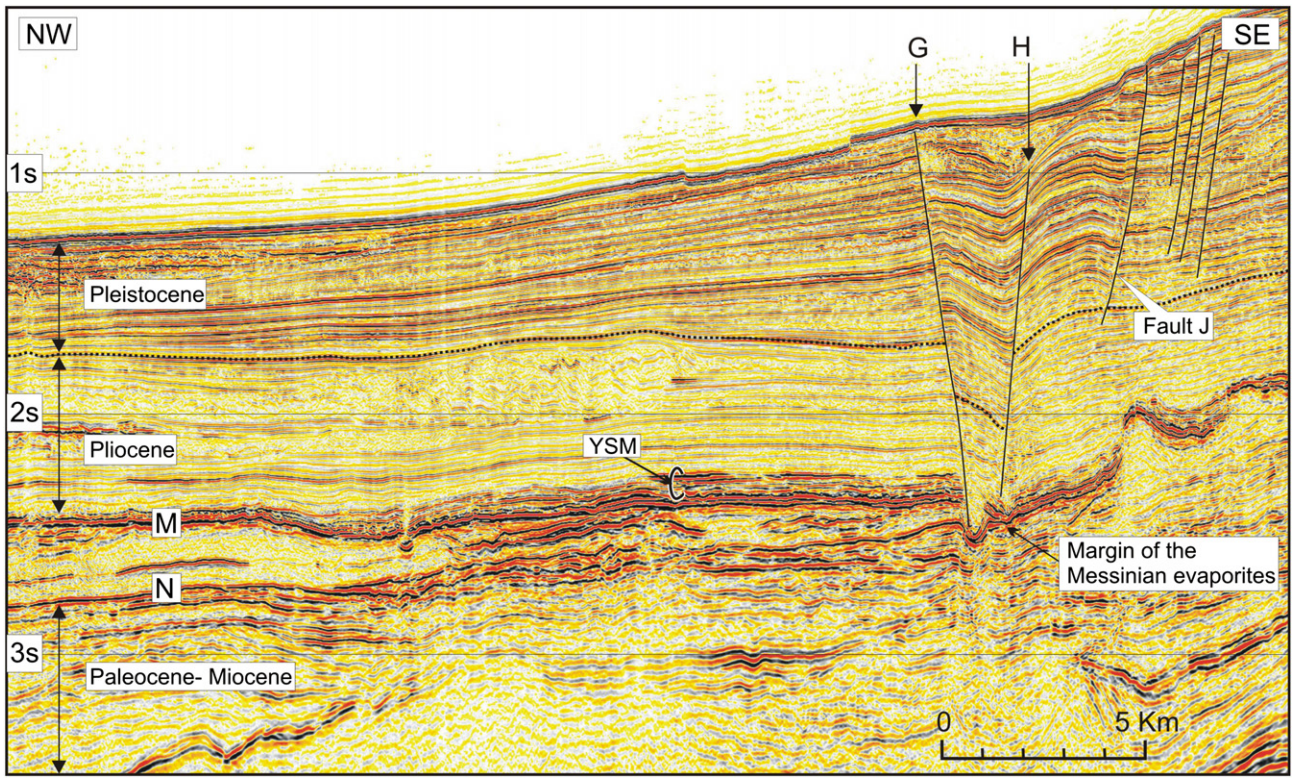

Fig. 2. Seismic regional section across the Levant Basin continental margin showing the main stratigraphic units. The Messinian evaporites are recognisable by the strong basal (N) and top (M) reflections and overlain by the Yafo Sand Member (YSM). The growth faults, located on the shelf break, and the Kefira graben system (composed of Faults G and H) are controlled by the pinch-out of the Messinian evaporites.

Schlumberger Geoframe 3.7 seismic interpretation software on a UNIX workstation. Horizons A–E are correlative markers within the Pleistocene succession, and were mapped to describe the structure and provide reference data for throw distributions. Detailed measurements of the throw values on faults were made using fault-normal seismic profiles. The throw measurements were displayed as individual plots of a single profile transect (*T–Z* plot, Cartwright et al., 1998; Baudon and Cartwright, 2008) and as contoured fault-plane projections of throw values derived from regularly spaced transects across the fault plane. The projection followed standard techniques outlined by Barnett et al. (1987).

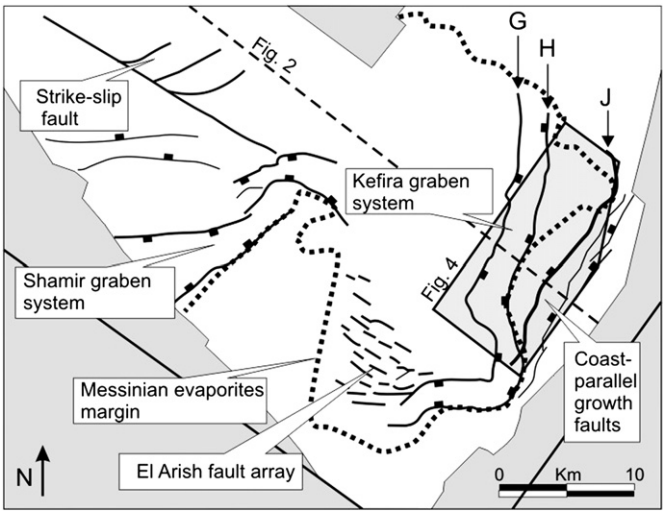

Fig. 3. Structural map of the Levant survey based on a Pleistocene Horizon.

We display throw values in two-way travel time (TWT), having established through careful depth conversion using the check-shot velocity data from the nearby control wells that vertical patterns of throw between depth-converted and TWT profiles do not differ significantly. Velocity varies only gradually vertically, and minimally laterally through the target interval, based on ten widely spaced control wells.

Correlation of stratigraphy between hangingwall and footwall was excellent and therefore minimised error in throw measurement. Errors in throw are attributed mainly to sampling of the seismic data, and are estimated to be 2 ms TWT (for detailed discussion of the sampling interval error, see Baudon and Cartwright, 2008). Errors linked to differential compaction between hangingwall and footwall sequence would only be significant in the case of sufficiently large throw values (e.g. Mansfield, 1996; Cartwright et al., 1998) and are therefore considered negligible for this study. Drag folds can also introduce errors into throw measurements (e.g. Walsh and Watterson, 1987; Mansfield and Cartwright, 1996), and true drag folds cannot generally be distinguished from seismic artefacts for fold wavelengths <2–3 times spatial resolution. Drag folds with wavelengths <100 m were therefore included in the throw measurements and these were made at inflection points (cf. Mansfield and Cartwright, 1996).

Throw measurements can be greatly influenced by lithological effects and the development of fault scarps (Cartwright et al., 1998; Castelltort et al., 2004; Back et al., 2006). We assume that thickness differences in syn-kinematic (growth) intervals between footwall and hangingwall equate to the throw accrued during that interval. This assumption is based on the sedimentation rate being equal to or greater than the slip rate (Cartwright et al., 1998), which is considered reasonable given the gross rate of progradation and aggradation of the shelf-slope system in the study area (Garfunkel and Almagor, 1985; Tibor and Ben-Avraham, 1992).

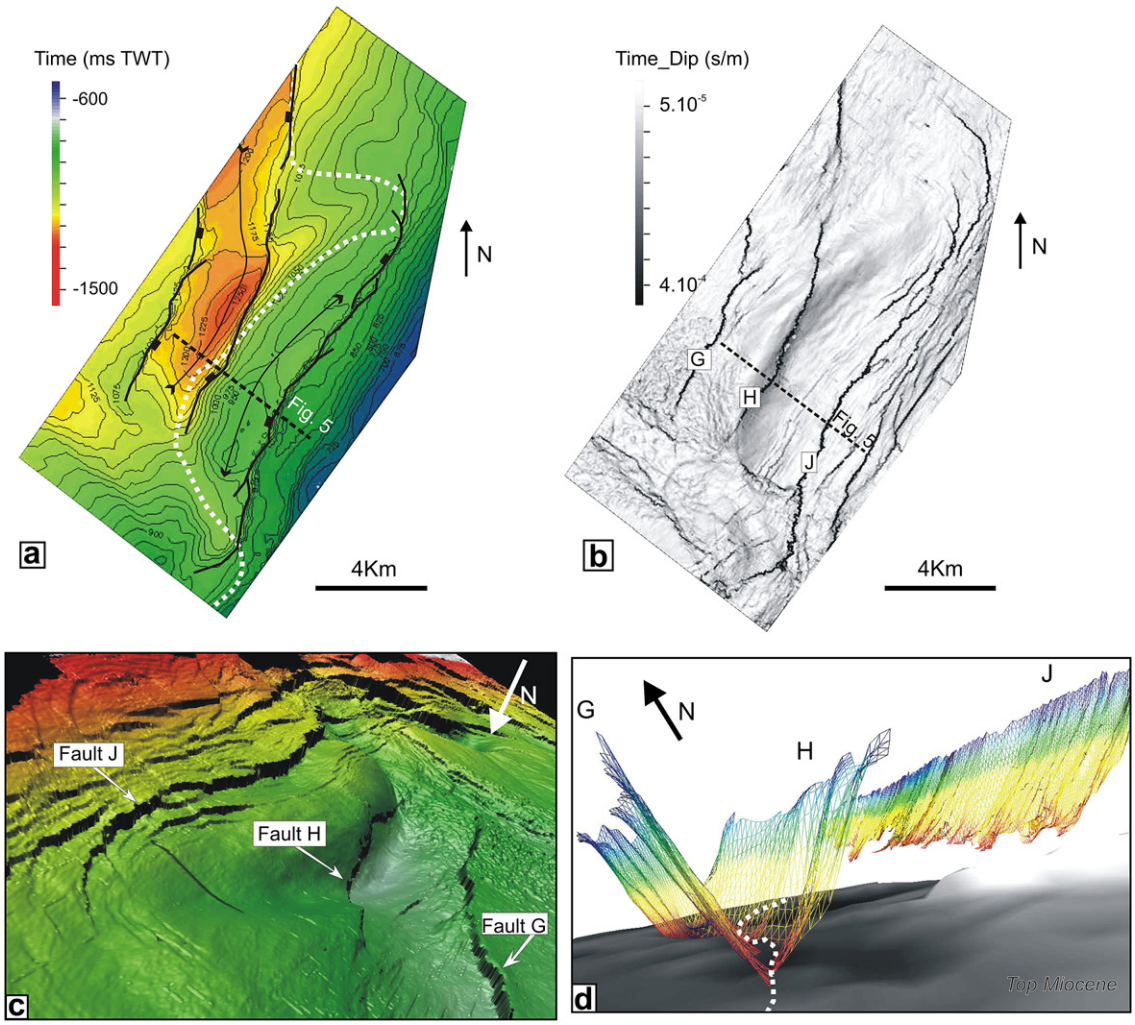

Fig. 4. Structural map of the area comprising the Kefira graben and the coast-parallel faults based on Pleistocene Horizon Ba (shown in Fig. 5). (a) Two-way time map showing contours spaced at 25 ms TWT with low values in red and high values in blue. The dashed line represents the edge of the Messinian evaporites. Arrows indicate syncline and anticline. (b) Dip map showing the traces of the main Faults G, H and J. (c) Geoviz image of Pleistocene Horizon Ba. (d) Geoviz visualisation of the geometry of Faults G, H and J related to the top Miocene.

3. 3D Seismic interpretation

The most prominent structures of the study area include the Shamir and Kefira Graben systems, which both detach into the Messinian evaporites, and a set of coast-parallel growth faults, one of the largest of which, Fault J, is the main focus of this study (Fig. 3). An array of blind normal faults (the El Arish Array in Baudon and Cartwright, 2008) forms a diffuse zone of minor deformation linking the two main grabens.

The Kefira Graben is located 4–5 km downslope from Fault J, and strikes NNE-SSW (Fig. 4a). This graben consists of two main conjugate syn-sedimentary faults (labelled G and H in Fig. 4). The timing of activity on Faults G and H is well constrained from growth indices and stratal geometry. Both growth faults exhibit fairly consistent stratigraphic thickening in the hangingwall, increasing with depth and throw gradients up to 0.85. Fault G exhibits a small scarp at the surface (<10 m) implying it is active at present, whereas Fault H terminates upward at stratigraphic levels situated between a few tens of metres and 200 m beneath the present-day seabed just above Horizon B (Figs. 2 and 5), implying it ceased activity in the late Pleistocene. The overlying long-wavelength hinge above Fault H (Fig. 5), is related to salt withdrawal, and is not upper-tip folding.

4. Fault J

4.1. Segmented geometry of Fault J

Fault J is a planar to gently listric normal fault that was selected for detailed description and analysis because it is the largest fault in an array of similar striking seaward-dipping growth faults located at the updip limit of the extensional domain of this basin margin (Figs. 4 and 5). Fault J strikes an average of 040° and dips at c. 55° toward the NW. The maximum length of the fault trace is c. 14 km and its maximum height is c. 1300 m, for a maximum throw of c. 125 m. Fault J is generally represented by a small scarp at the present day seabed (<10 m) confirming it is currently active, and tips out downward, and probably detaches within a stratigraphic interval situated between Pleistocene Horizon E and a few tens of metres beneath the Pliocene–Pleistocene boundary (P-P) (Fig. 5). The detachment geometry is not clear, and varies along strike, but is located approximately in an interval of slumping based on abrupt changes and pronounced rotations in hangingwall dip (Fig. 5).

Fault J is subdivided into three main segments (J1, J2, and J3) recognised from mapped changes in strike of the main fault plane and their association with splay faults that geometrically match breached relay structures (Trudgill and Cartwright, 1994). Five

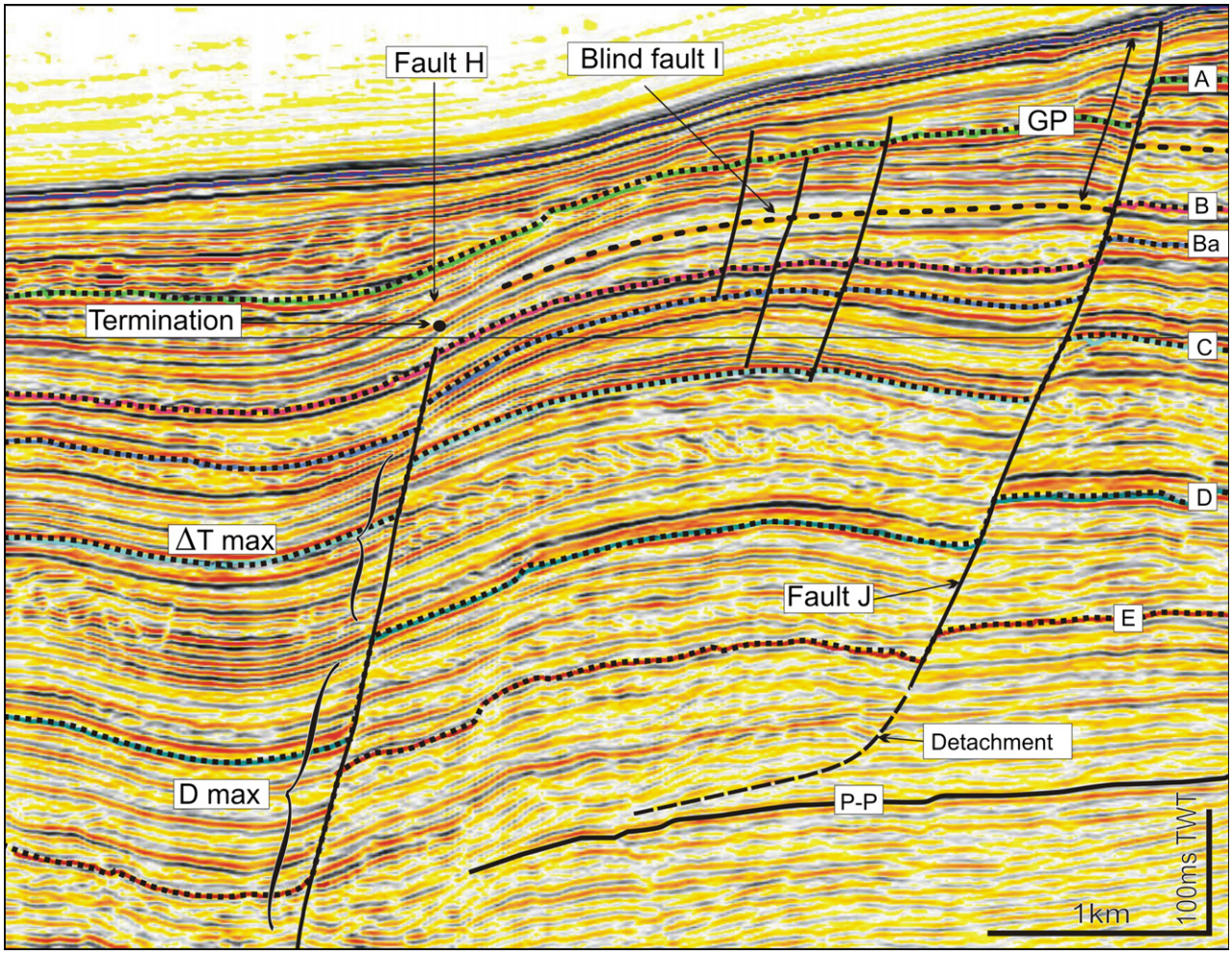

Fig. 5. Seismic section through Faults H and J showing the stratigraphy and key Pleistocene horizons (A, B, Ba, C, D and E). P-P marks the Pliocene–Pleistocene boundary. Stratigraphic thickening is expressed under the form of growth packages (GP) in the hangingwall of Fault J. The dashed line marks the base of the syn-kinematic sequence which corresponds to upper termination of Fault H. Zones of maximum throw gradients (ΔT) and displacement values (D_{max}) are indicated for Fault H.

branch lines (*v*–*v*′ to *z*–*z*′ on Fig. 6b,c) mark the location of these splay faults or interaction with other fault segments (Figs. 6 and 7). The throw distribution was compiled from 1753 throw measurements on cross sections taken orthogonal to the fault plane and spaced at 250–500 m.

4.2. Throw distribution on Fault J

The central parts of the throw contour plot consists of three main zones of large throw values (Fig. 6c) separated by vertical areas of smaller throw values. The larger throws (up to c. 125 ms TWT) occur in Segment J1 between branch lines *v*–*v*′ and *w*–*w*′ and are distributed as two smaller and interconnected zones of maximum throw. A second region of maximum throw is situated in Segment J2 between branch lines *w*–*w*′ and *x*–*x*′ and a third is located in Segment J3 between branch lines *y*–*y*′ and *z*–*z*′.

The throw variation over the upper tip region is characterised by closely spaced, horizontal to sub-horizontal throw contours (Fig. 6c). This geometry is comparable to the pattern typically seen on syn-sedimentary faults (Childs et al., 2003). The only branch lines with a present day surface expression are *x*–*x*′ and *y*–*y*′. The basal-tip region of Fault J is very irregular and lateral variations in basal-tip position and in contour patterns adjacent to the tip also correspond to the segmented structure (Fig. 6c). The basal tip only exhibits a clear basal detachment geometry for Segment J1.

The throw variation on the various splay or interacting faults linked to the main fault plane through the branch lines indicated on Fig. 6c is shown in Fig. 7. Throw contours for Splay J1b are in continuity with those of Segment J1 and decrease away from branch line *w*–*w*′ (Fig. 7b). Splay J3b exhibits contours decreasing away from branch line *y*–*y*′ (Figs. 6c and 7c). Splay J3a shares a common pattern of throw variation with main Segment J3, namely a crudely semi-elliptical pattern with maxima at branch line *z*–*z*′ (Fig. 7d). Segment J1a differs from the other splay faults in that its throw values decrease towards the intersection (Fig. 7a). This segment is linked to another fault and intersects Fault J with a high angle. To illustrate the vertical variations of throw distributions in more detail, throw versus depth plots were constructed along the length of Fault J. Throw measurements could be made vertically at closely spaced intervals of c. 20–30 m due to the high frequency content of the seismic data, thereby providing excellent resolution of subtle vertical variations. A subset of these *T*–*Z* plots is presented in Fig. 8.

Immediately adjacent to the lateral tips of Fault J, the vertical throw profiles are mesa shaped (M-type of Muraoka and Kamata, 1983) with an almost uniform throw distribution for >70–80% of the profile. In contrast, *T*–*Z* plots of the main part of the fault plane exhibit strongly asymmetric hybrid profiles consisting of three recognisable sections separated by breaks in gradient. First, the upper region is characterised by a high positive gradient (0.8–1.30) between the seabed and the point of the maximum throw value,

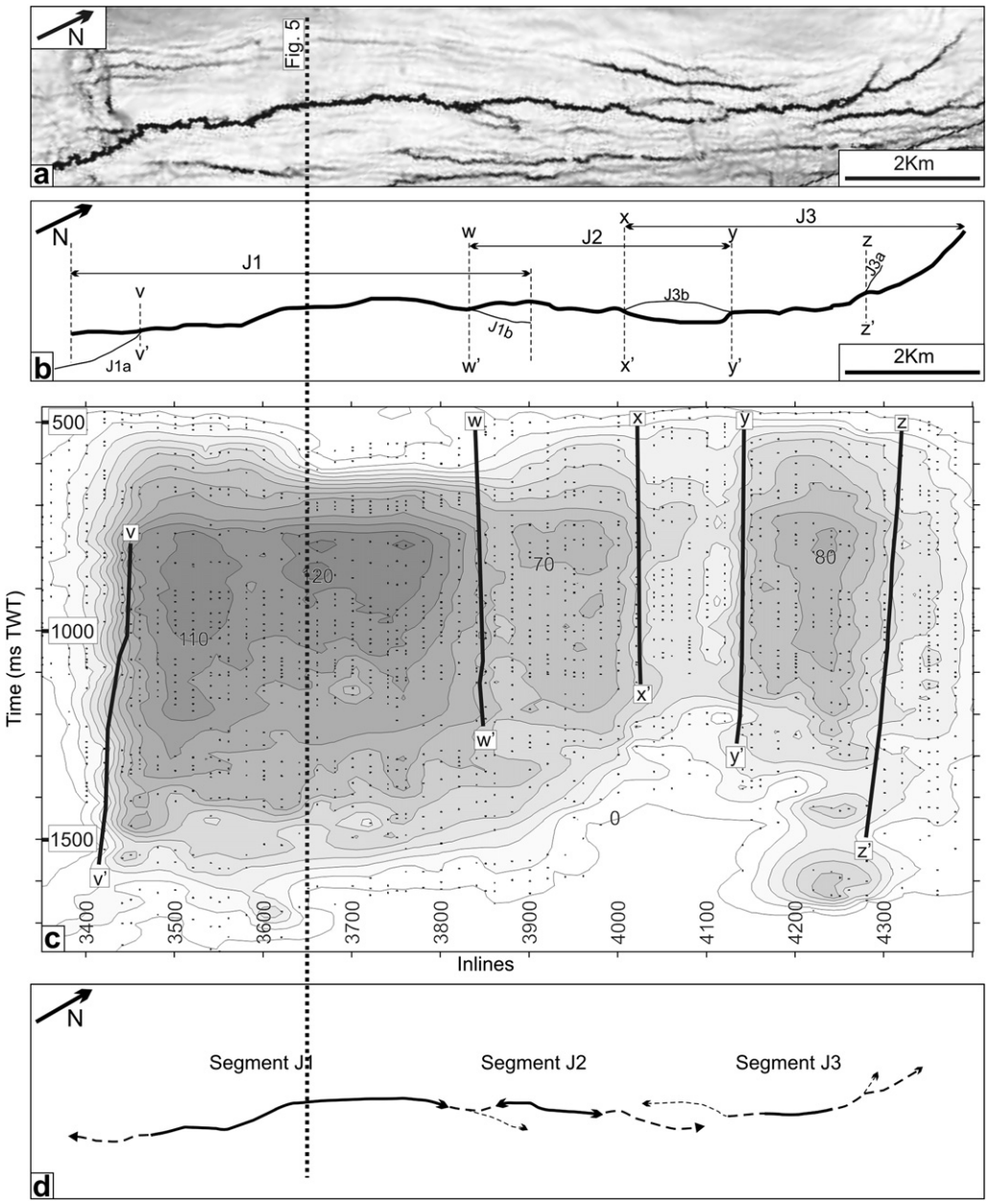

Fig. 6. (a) Dip map of Pleistocene Horizon D showing the trace of Fault J. (b) Schematic representation of the fault trace and names of different segments. (c) Throw contour plot for Fault J spaced every 10 ms TWT. (d) Cartoon showing the lateral segment linkage that formed Fault J.

generally located between Horizons A and B (Fig. 8). Second, the central region of the fault exhibits an almost constant negative slope with low average throw gradients (0.04–0.06) from the point of maximum displacement to an inflection point located in the lower third of the fault plane. The third and lower region is characterised by steeper negative average gradients (0.22–0.39) from the inflection point to the lower tip point.

4.3. Interpretation of throw distribution

Close inspection of the throw pattern in the upper region of the fault plane shows a number of intervals of large throw gradients with changes of slope and steps (e.g. profiles 7 and 12 on Fig. 8). These stepped profiles are similar to those compiled for small growth faults in the Gulf of Mexico (Cartwright et al., 1998), suggesting that the upper region is developed within the syn-kinematic portion of the stratigraphy, as is also suggested by the strongly horizontal throw contours on Fig. 6c. The base of the syn-kinematic package was estimated for each of the profiles where seismic data quality was great, using the established methodology of identifying stratal expansion and divergence (Thorsen, 1963; Edwards, 1995). To substantiate these observations, we mapped channels within the notional syn- and pre-kinematic packages using a coherency volume processed from our 3D seismic data, and found that channels were frequently diverted within the syn-kinematic package, whereas those in the pre-kinematic package were not (Fig. 9d,c, respectively). Channel diversion is known to be influenced by active faulting in comparable settings (Anderson et al., 2000).

Based on these observations, the stratigraphic markers defining the base of the syn-kinematic package for each profile position were plotted on the *T*–*Z* profiles (Fig. 8). These were recorded for 11

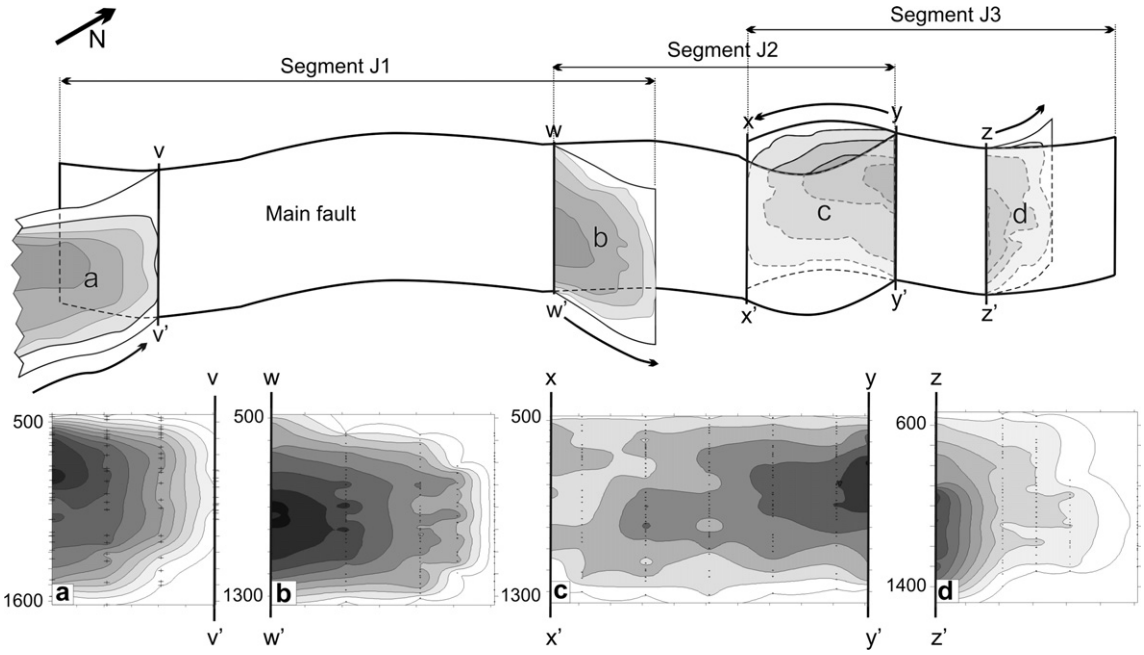

Fig. 7. (Top) Segmented 3D geometry of Fault J (segments labelled J1, J2 and J3), and its relationships with fault splays or bifurcation of the fault plane. Arrows showing decreasing throw values indicate the direction of propagation of the fault segments. (Bottom) Throw contour plots showing lines of equal throw values: (a) The throw values for Segment J1a range from 0 to 110 ms TWT (represented by dark colour) with contours spaced every 10 ms TWT. (b) Throw contour plot for Segment J1b exhibits throw values ranging from 0 to 16 ms TWT decreasing away from the branch line, and contour spacing of 2 ms TWT. (c) Throw distribution on the hangingwall splay (J3b) of the relay zone shows throw values ranging from 0 to 30 ms TWT, contours spaced at 5 ms TWT. (d) Throw contours plot for Segment J3a showing throw values ranging from 0 to 45 ms TWT and spaced at 5 ms TWT decreasing away from the branch line.

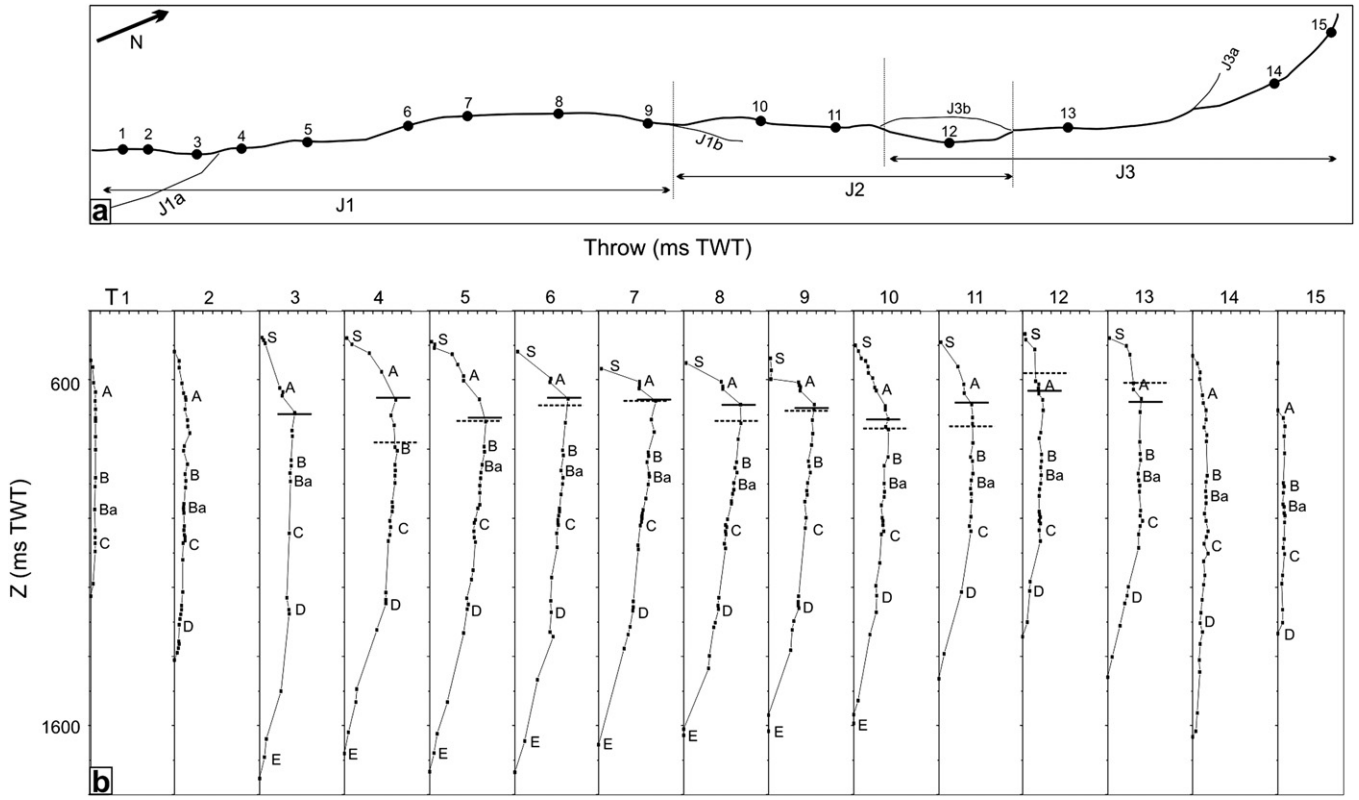

Fig. 8. (a) Schematic fault trace of Fault J based on the Pleistocene Horizon D with location of the 15 *T*–*Z* plots. (b) Vertical throw distribution plots for 15 representative sections of Fault J. Throw values (*T*) on the horizontal axis, are up to 140 ms TWT, plotted against the time (*Z*) in ms TWT on the vertical axis. Horizontal lines represent the base of growth packages across the fault plane and the dashed lines represent the stratigraphic interval in which G2 became inactive.

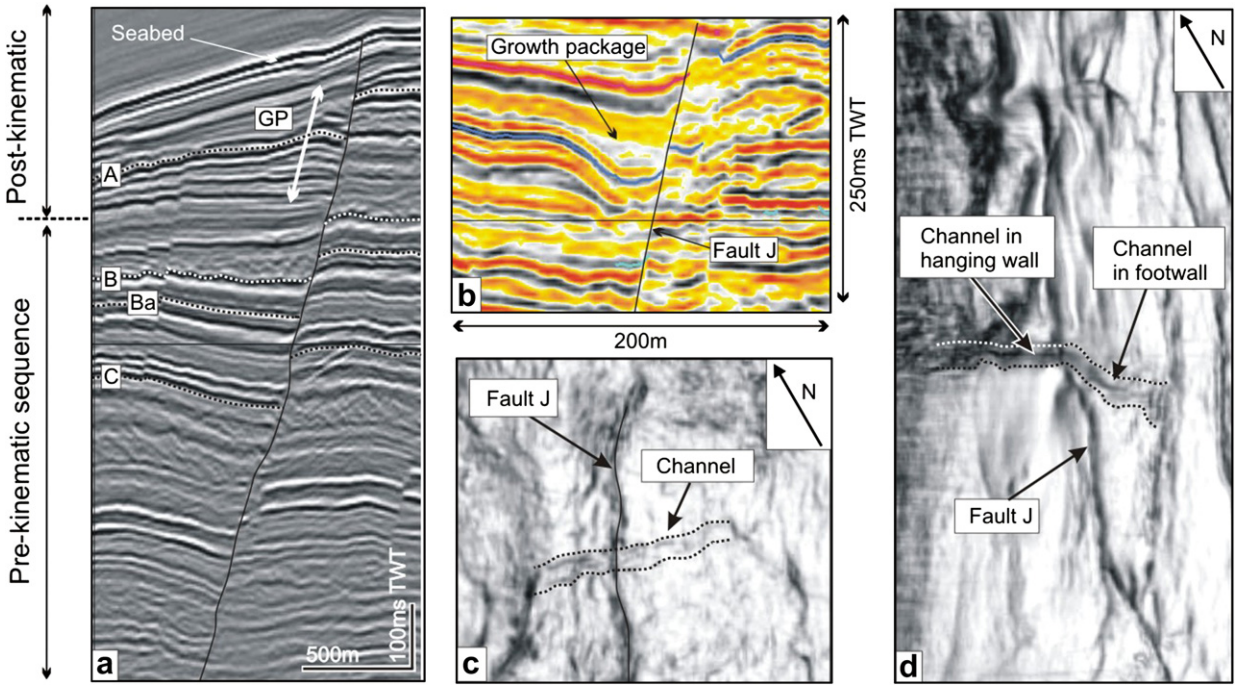

Fig. 9. (a) Seismic cross-section showing the stratigraphic thickening in the hangingwall within the syn-kinematic sequence. GP indicates the growth packages. (b) Seismic section showing a growth package in the hangingwall of Fault J in the syn-kinematic sequence. (c) Coherency slice at 1416 ms TWT showing a channel cross-cut by Fault J within the pre-kinematic sequence. The size, direction and geometry of the channel are unchanged. (d) Coherency slice at 528 ms TWT showing the change of direction of a channel being cross-cut by Fault J.

out of the 15 profiles, and occur between Horizons A and B. Slight apparent younging of the stratigraphic position of this marker occurs between Segments J1/J2 and J3, but this diachroneity amounts to no more than 2 or 3 reflections, which based on average sedimentation rates, amounts to probably $<$100 ka. It is striking that this stratigraphic marker corresponds closely to the maximum throw position in the *T*–*Z* profiles (Fig. 8).

The onset of syn-sedimentary growth for Fault J in the interval delimited by Horizons A and B is interesting when viewed in a semi-regional context. Fault J is just a few kilometres upslope from the eastern boundary fault (Fault H) of the Kefira Graben (Fig. 4). This fault ceased to be active early in this A–B interval. Correlation of the reflection marking the upper tip of this fault into the hangingwall of Fault J (Fig. 5), shows that cessation on Fault H preceded the onset of syn-sedimentary growth by a short interval of time equivalent to 30–50 m thick group of reflections (illustrated by the horizontal lines on Fig. 8). We therefore suggest that the kinematic behaviour of the two faults was coupled, such that termination of the downslope fault's activity resulted in the locus of active slip switching to that upslope. Similar kinematic interdependence has been observed in sub-parallel arrays of gravity-driven fault systems elsewhere (Cartwright et al., 1998). This coupling might involve physical connection of the detachment of Segment J1 with Fault H, but this geometry cannot be confirmed from the seismic data.

Segments J1, J2 and J3 are characterised by zones of maximum throw value separated by vertical zones of throw minima. This pattern is typical of segmented faults that have grown by radial propagation and subsequent linkage at relay structures (Peacock and Sanderson, 1991; Walsh and Watterson, 1991; Cartwright et al., 1995; Dawers and Anders, 1995; Walsh et al., 2003). Fault J is therefore interpreted as resulting from the growth and coalescence of J1, J2 and J3, with the splay faults observed at the changes in fault strike being typical remnants of earlier hard linkage and relay abandonment. In addition, the subtle subdivision of Segment J1 into two discrete throw maxima suggests that it grew from the early linkage of two smaller segments without a relay zone or branch line being preserved. Another zone of large throw is located in the lower tip of Segment J3 (Fig.6c) and is interpreted to be due to a linkage of the lower tip of the main fault plane with a small fault at depth.

The linkage history of the three main segments is interpreted with reference to the splay or interacting faults (e.g. Childs et al., 1996; Nelson, 2007). The decrease in throw on Segment J1a towards the zone of intersection with the main fault plane at branch line *v*–*v*′ (Fig. 7a), is interpreted as a separate fault that propagated towards Fault J. The throw pattern for Splay J1b (Fig. 7b) is interpreted as being the breached NE tip of Segment J1 as no clear cut-off in the throw distribution is observed between Segment J1 and Splay J1b through the branch line. Segments J2 and J3 connect with each other through a doubly breached relay zone (Trudgill and Cartwright, 1994) with Splay J3b as the breached former tip zone of Segment J3. Segment J3a is interpreted as a splay as it shares a northward direction of decreasing throw with the main Segment J3 away from branch line *z*–*z*′ (Fig. 7d). Similar fault-plane geometry and associated throw patterns have been interpreted to result from the bifurcation of main fault plane during lateral propagation (Childs et al., 1996; Marchal et al., 2003; Nelson, 2007).

In summary, Fault J is interpreted as resulting from the combination of hard linkage of 3 main segments through breached relay zones and a lateral bifurcation of the fault plane, followed by a growth history as a single linked, segmented fault. The base of the syn-kinematic interval defined on the seismic data corresponds to the transition from a sub-vertical to dominantly horizontal throw contour pattern (Fig. 6c) as shown for other syn-sedimentary faults (Childs et al., 2003). The onset of syn-sedimentary faulting occurred at some time between Horizons A and B, possibly triggered by cessation of motion on Fault H.

5. Discussion

Modern studies of the displacement distribution on normal faults commonly infer that the locus of the nucleation coincides with the region of the maximum displacement (e.g. Walsh and Watterson, 1987; Wilkins and Gross, 2002). Blind normal faults, for example, are classic illustrations of this concept, whereby the apex of idealised C-shaped displacement distributions represents the nucleation site (Barnett et al., 1987; Walsh and Watterson, 1987; Nicol et al., 1996). For syn-sedimentary faults, a significant change in the gradient of the throw profile indicates the onset of faulting and that the faults initiated within areas of maximum throw values (Childs et al., 1993; Meyer et al., 2002).

T–Z profiles for Fault J (Fig. 8) all show that the point of maximum throw on each profile coincides with the base of the syn-kinematic package. Applying the general concept of nucleation at the point of maximum throw, this arrangement would place the point of nucleation at the free surface during the interval Horizon A–B. From this interpretation, it follows that the fault would have accumulated syn-kinematic (growth) sequences above the nucleation point whilst propagating laterally and downward toward the present-day position of the lower tip-line (Fig. 10a).

Several problems exist for this initiation model. First, although not physically impossible, it is unlikely that shear fractures first formed at or close to the free surface. The near-surface sediments in this basin are clay-rich, have high porosity, and low shear strength (Almagor, 1986), and are much more likely to deform in a ductile manner than localise shear fractures of any size. Second, gravitational driving stresses would be maximised near the major basal detachment for the extensional domain at the top of the Messinian evaporites (Schultz-Ela and Walsh, 2002), so nucleation might be more reasonably expected to occur at depth. Third, the basin lacks modern analogues of faults that nucleated at surface and propagated in a semi-elliptical geometry downward and sideward.

An alternative model for the growth of Fault J (Fig. 10b) is that it initiated as a series of blind fault segments, which propagated radially, linked and continued to grow as a single fault. At some point in this evolution, the upper tips reach the free surface during active sedimentation and the fault switched from being blind to a syn-sedimentary growth mode, which is marked by the onset of syn-kinematic stratigraphic expansion across the upper tip. Also, most displacement accumulated during the syn-kinematic period. This second fault-growth model is supported by three main lines of evidence:

1. The geometry of the three main Segments J1, J2 and J3 points to a phase of blind propagation prior to the onset of syn-sedimentary growth. The segment boundaries coincide with clustering of vertical throw contours (Fig. 6c), consistent with lateral linkage models (Walsh et al., 2003).
2. The upper-tip line of Fault J gradually plunges several hundred metres within the lateral tip regions. This geometry suggests that the lateral tips propagated blind at least during their latest stages of growth (Childs et al., 2003; Baudon and Cartwright, 2008). This type of lateral-tip geometry is more simply explained by blind growth of the lateral tips than by surface nucleation of the fault and inward migration of the lateral tips during the latest stages of growth.
3. Nearby faults exhibiting all the hallmarks of exclusively blind propagation are found within the extensional domain downdip from Fault J, with throw maxima located in the B–C interval (Fig. 5). Faults in the El Arish array some 10–15 km west of Fault J are also classical blind structures, with throw maxima in the B–D interval. These faults all exhibit M-type *T–Z* profiles, with remarkably little change of throw over their central portions (Baudon and Cartwright, 2008). The presence nearby of numerous blind faults within the B–D interval raises the likelihood that Fault J also commenced its growth in the same way, and in the same interval, because of the common driving gravitational state, and laterally uniform mechanical properties in the Pleistocene clay-dominated slope sediments.

Based on these three lines of evidence combined with the problems for the first model, we select the second model as applicable. Can we next infer anything about the relative timing of the blind stage and the syn-sedimentary stage from any of the data about throw distribution? Throw distributions provide mere snapshots in fault evolution, and backstripping them to infer an evolutionary sequence is full of pitfalls, and usually requires a predetermined set of assumptions to be applied. However, if

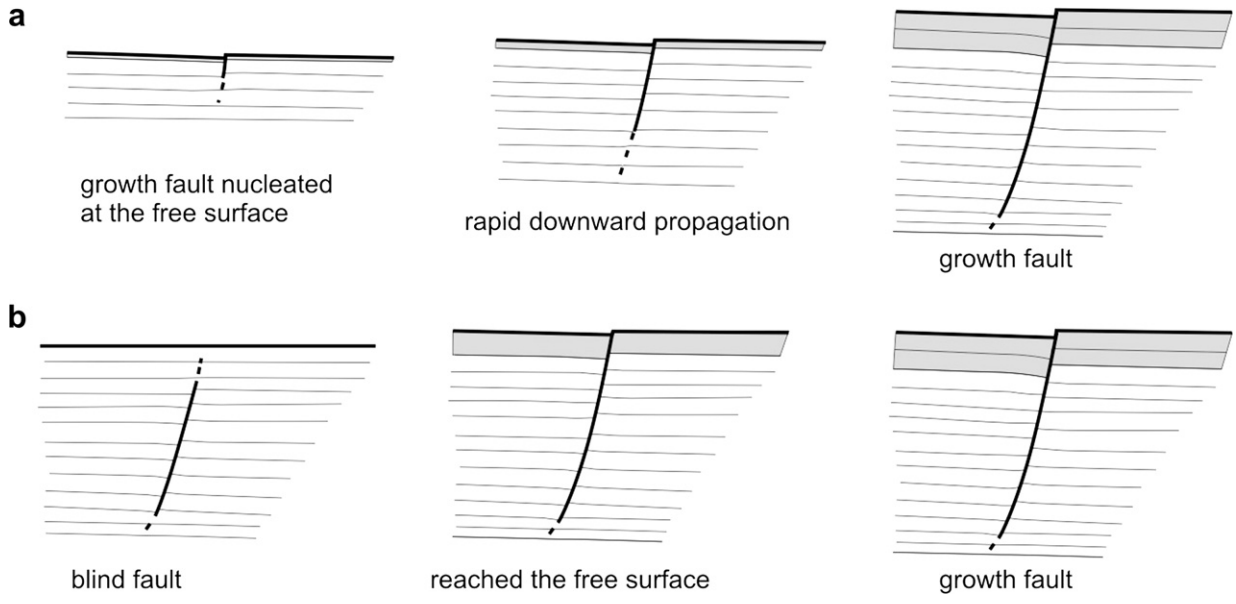

Fig. 10. Two different models of growth for Fault J. (a) Nucleation of the fault at the free surface and accumulation of the syn-sedimentary interval (shaded area) whilst rapid downward propagation of the lower tip. (b) Nucleation as a blind fault which reached the surface and become a growth fault in a later stage of evolution.

we accept model 2 as realistic, then we can potentially use throw distribution data from the neighbouring blind faults to provide some basic constraints as to the likely growth history of Fault J.

Fig. 11a shows a representative selection of *T–Z* profiles from the central portions of the nearest neighbouring blind faults (Fig. 5, Fault I and adjacent faults). This combined plot shows that the typical blind fault has a profile close to an M-type than a C-type, with very gentle throw gradients in the central portions. If we take a best fit to these, and cross plot it with a *T–Z* profile from the centre of Fault J, we can then visualise the additional throw required to evolve from this idealised blind stage to the present day syn-sedimentary stage. It is worth noting that the blind profiles of Fig. 11a are strikingly similar to profiles 1, 2, 14 and 15 at the lateral tip regions of Fault J. We suggest that lateral-tip regions represent an early stage in the propagation history, and they may therefore offer insight into the earlier accumulation of throw in the centre of each segment (Fig. 11b).

Comparing the throw profiles, the near-zero gradient of the central part of the blind fault evolved into a gentle negative throw gradient after seabed interaction, which could mean for Fault J, that incremental additions of throw aggregated to create a downward throw decrease and hence, negative gradient. This evolution suggests that throw is not added uniformly as the blind fault makes the transition to a fully syn-sedimentary fault.

Also, the maximum throw to height ratio of the blind fault is much less than for Fault J. This is also true for the strike-length of Fault J, which is similar to the cumulative length of the original blind segments, although the throw increased between five- and ten-fold. The growth of Fault J therefore follows a non-linear evolution of displacement versus dimension (vertical and horizontal). This non-linear scaling path should be distinguished from other recent studies of non-linear fault growth where displacement can be added for a near constant length as lateral tips interact between neighbouring faults or where propagation is guided by the up-dip reactivation of pre-existing underlying structures (e.g. Meyer et al., 2002; Walsh et al., 2002). In our study, we suggest that this non-linearity arises because of the change in propagation mode from blind to syn-sedimentary growth.

The final point that arises from this discussion is that the point of maximum throw on the final profile is unlikely to be maintained during the transition from blind to syn-sedimentary stages of growth (Fig. 11b).

Finally, the nucleation position for the typical blind faults around Fault J is in the B–C interval, assuming correspondence to the maximum throw position (Watterson, 1986; Barnett et al., 1987). However, the maximum throw is in the A–B interval for Fault J, which is several hundred metres shallower in the section. Some previous studies have indicated that the maximum throw position for syn-sedimentary faults would be the nucleation position (Childs et al., 1993; Meyer et al., 2002), but our analysis challenges this view, at least based on the application of model 2 to Fault J. Other studies have previously suggested that the point of maximum displacement can migrate away from the point of nucleation of the fault (Peacock, 1991), which is consistent with our observations if the blind faults are assumed to be earlier stages of Fault J. This has been attributed to interactions with other faults or variations in elastic properties (Burgmann et al., 1994; Cowie, 1998; Cowie and Shipton, 1998; Maerten et al., 1999; Schultz, 2000) or mechanical barriers (e.g. Wilkins and Gross, 2002). We suggest also including the interaction with the free surface during the transition from blind to syn-sedimentary activity as a factor. The point of maximum displacement is unlikely to be maintained during the transition from blind to syn-sedimentary faulting.

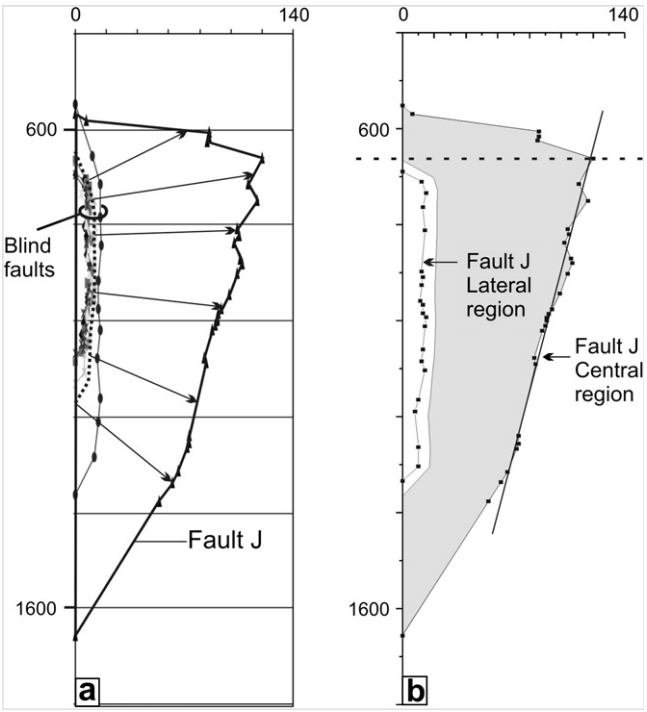

Fig. 11. (a) Vertical throw profiles from the central portions of Fault J and for the nearest neighbouring blind faults. Dashed line represents the best fit to the profiles obtained for blind faults and arrows indicate possible growth paths (b) Vertical throw profile on the central region and lateral tip region of Fault J. The dashed line marks the limit between pre-faulting and syn-faulting sequences.

6. Conclusions

(1) A gravity-driven growth fault (Fault J), located on the Levant passive continental margin, is interpreted as resulting from the radial propagation of the precursor blind fault segments, hard linkage of these individual segments with bifurcations of the fault plane, and single fault development growth faulting.

(2) *T–Z* plots for this fault exhibit M-type profiles at the lateral tip regions and skewed M-type on the central portions. The skewed M-type consists of an upper part characterised by large positive throw gradients associated with growth packages and is interpreted as the syn-kinematic interval. The base of this interval is within a few tens of metres of a single datum along the strike length, with only minor younging visible in the northern segment. The central portion of the throw profiles is marked by almost constant and low negative throw gradients. A lower portion is marked by steeper negative gradients.

(3) Fault J is considered to have initiated as a blind fault that subsequently reached the sediment–water interface and became a syn-sedimentary fault, based on the throw contour pattern at the linkage positions, comparisons with neighbouring blind faults, and the recognition of a plunging upper tip line.

(4) The interaction of the fault plane with the free surface resulted in a probable shift in the accumulation of throw on the fault surface, changing the position of the point of maximum displacement.

(5) Most of the surface area of the fault was established early in the growth history during blind propagation, as the three precursor segments became hard linked. Non-linear accumulation of displacement and length is represented by the much larger ratio (5–10 times greater) of throw to length for the syn-sedimentary than the blind stage.

Acknowledgements

We wish to thank BG-Group for supplying the seismic data and permission to publish this work. In particular, help from Paul Griffiths is greatly appreciated. Schlumberger Ltd is acknowledged for providing Geoquest seismic interpretation software. This paper benefited from discussions with various colleagues from the 3D Lab and especially Mairi Nelson, Simon Higgins and David James. Brent Couzens-Shultz, Jon Bull and Editor William M. Dunne are thanked for thoughtful and constructive reviews which greatly improved the manuscript.

References

Almagor, G., 1986. Mass transport on the continental slope of Israel. Geo-Marine Letters 6, 29–34.

Anderson, J.E., Cartwright, J.A., Drysdall, J., Vivian, N., 2000. Controls on turbidite sand deposition during gravity-driven extension of a passive margin: example from Miocene sediments in Block 4, Angola. Marine and Petroleum Geology 17 (10), 1165–1203.

Back, S., Hocker, C., Brundiers, M.B., Kukla, P.A., 2006. Three-dimensional-seismic coherency signature of Niger Delta growth faults: integrating sedimentology and tectonics. Basin Research 18 (3), 323–337.

Barnett, J.A.M., Mortimer, J., Rippon, J.H., Walsh, J.J., Watterson, J., 1987. Displacement geometry in the volume containing a single normal fault. American Association of Petroleum Geologists Bulletin 71 (8), 925–937.

Baudon, C., Cartwright, J.A., 2008. 3D seismic characterisation of an array of blind normal faults in the Levant Basin, Eastern Mediterranean. Journal of Structural Geology 30 (6), 746–760.

Bertoni, C., Cartwright, J.A., 2006. Controls on the basinwide architecture of late Miocene (Messinian) evaporites on the Levant margin (Eastern Mediterranean). Sedimentary Geology 188-189, 93–114.

Bruce, C.H., 1973. Pressured shale and related sediment deformation: mechanism for development of regional contemporaneous faults. American Association of Petroleum Geologists Bulletin 57 (5), 878–886.

Burgmann, R., Pollard, D.D., Martel, S.J., 1994. Slip distributions on faults: effects of stress gradients, inelastic deformation, heterogeneous host-rock stiffness, and fault interaction. Journal of Structural Geology 16 (12), 1675–1690.

Cartwright, J.A., Jackson, M.P.A., 2008. Initiation of gravitational collapse of an evaporite basin margin: the Messinian saline giant, Levant Basin, Eastern Mediterranean. Geological Society of America Bulletin 120, 399–413.

Cartwright, J.A., Trudgill, B.D., Mansfield, C.S., 1995. Fault growth by segment linkage: an explanation for scatter in maximum displacement and trace length data from the Canyonlands Grabens of SE Utah. Journal of Structural Geology 17 (9), 1319–1326.

Cartwright, J.A., Bouroullec, R., James, D., Johnson, H.D., 1998. Polycyclic motion history of some Gulf Coast growth faults from high-resolution displacement analysis. Geology 26 (9), 819–822.

Castelltort, S., Pochat, S., Van Den Driessche, J., 2004. Using T-Z plots as a graphical method to infer lithological variations from growth strata. Journal of Structural Geology 26 (8), 1425–1432.

Childs, C., Easton, S.J., Vendeville, B.C., Jackson, M.P.A., Lin, S.T., Walsh, J.J., Watterson, J., 1993. Kinematic analysis of faults in a physical model of growth faulting above a visous salt analogue. Tectonophysics 228, 313–329.

Childs, C., Nicol, A., Walsh, J.J., Watterson, J., 1996. Growth of vertically segmented normal faults. Journal of Structural Geology 18 (12), 1389–1397.

Childs, C., Nicol, A., Walsh, J.J., Watterson, J., 2003. The growth and propagation of synsedimentary faults. Journal of Structural Geology 25, 633–648.

Cowie, P.A., 1998. A healing-reloading feedback control on the growth rate of seismogenic faults. Journal of Structural Geology 20 (8), 1075–1087.

Cowie, P.A., Shipton, Z.K., 1998. Fault tip displacement gradients and process zone dimensions. Journal of Structural Geology 20 (8), 983–997.

Crans, W., Mandl, G., Haremboure, J., 1980. On the theory of growth faulting: a geomechanical delta model based on gravity sliding. Journal of Petroleum Geology 2 (3), 265–307.

Dawers, N.H., Anders, M.H., 1995. Displacement-length scaling and fault linkage. Journal of Structural Geology 17 (5), 607–614.

Druckman, Y., Buchbinder, B., Martinotti, G.M., Tov, R.S., Aharon, P., 1995. The buried Afiq Canyon (eastern Mediterranean, Israel): a case study of a Tertiary submarine canyon exposed in Late Messinian times. Marine Geology 123 (3-4), 167–185.

Edwards, M.B., 1995. Differential subsidence and preservation potential of shallow-water Tertiary sequences, northern Gulf Coast Bain, USA. In: Plint, A.G. (Ed.), International Association of Sedimentologists Special Publication. Sedimentary Facies Analysis 22, pp. 265–281.

Frey Martinez, J., Cartwright, J.A., Hall, B., 2005. 3D seismic interpretation of slump complexes: examples from the continental margin of Israel. Basin Research 17, 83–108.

Garfunkel, Z., 1998. Constrains on the origin and history of the Eastern Mediterranean basin. Tectonophysics 298 (1-3), 5–35.

Garfunkel, Z., Almagor, G., 1985. Geology and structure of the continental margin off northern Israel and the adjacent part of the Levantine basin. Marine Geology 62, 105–131.

Garfunkel, Z., Almagor, G., 1987. Active salt dome development in the Levant Basin, southeast Mediterranean. In: Lerche, I., O'Brien, J.J. (Eds.), Dynamical Geology of Salt and Related Structures. Academic Press, New York, pp. 263–300.

Hsü, K.J., Montadert, L., Bernoulli, D., Cita, M.B., Erickson, A., Garrison, R.E., Kidd, R.B. , Mélière, F., Muller, C., Wright, R.H., 1978. Initial Reports of the Deep Sea Drilling Project. 42. US Government Printing Office, Washington, DC. 1249.

Maerten, L., Willemse, E.J.M., Pollard, D.D., Rawnsley, K., 1999. Slip distributions on intersecting normal faults. Journal of Structural Geology 21, 259–271.

Mansfield, C.S., 1996. Fault growth by segment linkage. PhD thesis, University of London.

Mansfield, C.S., Cartwright, J.A., 1996. High resolution fault displacement mapping from three-dimensional seismic data: evidence for dip linkage during fault growth. Journal of Structural Geology 18 (2/3), 249–263.

Marchal, D., Guiraud, M., Rives, T., 2003. Geometric and morphologic evolution of normal fault planes and traces from 2D to 4D data. Journal of Structural Geology 25 (1), 135–158.

Meyer, V., Nicol, A., Childs, C., Walsh, J.J., Watterson, J., 2002. Progressive localisation of strain during the evolution of a normal fault population. Journal of Structural Geology 24 (8), 1215–1231.

Morewood, N.C., Roberts, G.P., 1999. Lateral propagation of the surface trace of the South Alkyonides normal fault segment, central Greece: its impact on models of fault growth and displacement-length relationships. Journal of Structural Geology 21 (6), 635–652.

Muraoka, H., Kamata, H., 1983. Displacement distribution along minor fault traces. Journal of Structural Geology 5 (5), 483–495.

Nelson, M., 2007. 3D geometry and kinematics of non-colinear fault intersections. Unpublished thesis, Cardiff University.

Netzeband, G.L., Hubscher, C.P., Gajewski, D., 2006. The structural evolution of the Messinian evaporites in the Levantine Basin. Marine Geology 230 (3-4), 249–273.

Nicol, A., Watterson, J., Walsh, J.J., Childs, C., 1996. The shapes, major axis orientations and displacement patterns of fault surfaces. Journal of Structural Geology 18 (2/3), 235–248.

Nicol, A., Walsh, J., Berryman, K., Nodder, S., 2005. Growth of a normal fault by the accumulation of slip over millions of years. Journal of Structural Geology 27 (2), 327–342.

Ocamb, R.D., 1961. Growth faults of south Louisiana. Transactions Gulf Coast Association of Geological Societies 11, 139–175.

Peacock, D.C.P., 1991. Displacements and segment linkage in strike-slip fault zones. Journal of Structural Geology 13 (9), 1025–1035.

Peacock, D.C.P., Sanderson, D.J., 1991. Displacements, segment linkage and relay ramps in normal fault zones. Journal of Structural Geology 13 (6), 721–733.

Petersen, K., Clausen, O.R., Korstgard, J.A., 1992. Evolution of a salt-related listric growth fault near the D-1 well, block 5605, Danish North Sea: displacement history and salt kinematics. Journal of Structural Geology 14 (5), 565–577.

Poulimenos, G., 2000. Scaling properties of normal fault populations in the western Corinth Graben, Greece: implications for fault growth in large strain settings. Journal of Structural Geology 22 (3), 307–322.

Schultz, R.A., 2000. Fault-population statistics at the Valles Marineris Extensional Province, Mars: implications for segment linkage, crustal strains, and its geodynamical development. Tectonophysics 316 (1-2), 169–193.

Schultz-Ela, D.D., Walsh, P., 2002. Modeling of grabens extending above evaporites in Canyonlands National Park, Utah. Journal of Structural Geology 24 (2), 247–275.

Thorsen, C.E., 1963. Age of growth faulting in the southeast Louisiana. Transactions Gulf Coast Association of Geological Societies 13, 103–110.

Tibor, G., Ben-Avraham, Z., 1992. Late Tertiary seismic facies and structures of the Levant passive margin off central Israel, eastern Mediterranean. Marine Geology 105, 253–273.

Tibor, G., Ben-Avraham, Z., 2005. Late Tertiary paleodepth reconstruction of the Levant margin off Israel. Marine Geology 221 (1-4), 331–347.

Trudgill, B.D., Cartwright, J.A., 1994. Relay ramp forms and normal fault linkages, Canyonlands National Park, Utah. Bulletin of the Geological Society of America 106, 1143–1157.

Vetel, W., Le Gall, B., Walsh, J.J., 2005. Geometry and growth of an inner rift fault pattern: the Kino Sogo Fault Belt, Turkana Rift (North Kenya). Journal of Structural Geology 27 (12), 2204–2222.

Walsh, J.J., Watterson, J., 1987. Distributions of cumulative displacement and seismic slip on a single normal fault surface. Journal of Structural Geology 9 (8), 1039–1046.

Walsh, J.J., Watterson, J., 1991. Geometric and kinematic coherence and scale effects in normal fault systems. In: Roberts, A.M., Yielding, G., Freeman, B. (Eds.), The Geometry of Normal Faults. Geological Society of London, Special Publication 56, pp. 193–203.

Walsh, J.J., Nicol, A., Childs, C., 2002. An alternative model for the growth of faults. Journal of Structural Geology 24, 1669–1675.

Walsh, J.J., Bailey, W.R., Childs, C., Nicol, A., Bonson, C.G., 2003. Formation of segmented normal faults: a 3-D perspective. Journal of Structural Geology 25, 1251–1262.

Watterson, J., 1986. Fault dimensions, displacements and growth. Pure and Applied Geophysics 124 (1/2), 365–373.

Wilkins, S.J., Gross, M.R., 2002. Normal fault growth in layered rocks at Split Mountain, Utah: influence of mechanical stratigraphy on dip linkage, fault restriction and fault scaling. Journal of Structural Geology 24 (9), 1413–1429.